# Abiotic synthesis of amino acids in the recesses of the oceanic lithosphere

Bénédicte Ménez, Céline Pisapia, Muriel Andreani, Frederic Jamme, Quentin Vanbellingen, Alain Brunelle, Laurent Richard, Paul Dumas, Matthieu Réfrégiers

# Abiotic synthesis of amino acids in the recesses of the oceanic lithosphere

Bénédicte Ménez[1], Céline Pisapia[1,2], Muriel Andreani[3], Frédéric Jamme[2], Quentin P. Vanbellingen[4], Alain Brunelle[4], Laurent Richard[5], Paul Dumas[2] & Matthieu Réfrégiers[2]

**Abiotic hydrocarbons and carboxylic acids are known to be formed on Earth, notably during the hydrothermal alteration of mantle rocks. Although the abiotic formation of amino acids has been predicted both from experimental studies and thermodynamic calculations, its occurrence has never been demonstrated in terrestrial settings. Using an innovative multimodal approach combining high-resolution imaging techniques, we obtain the first evidence for the occurrence of aromatic amino acids formed abiotically and subsequently preserved at depth beneath the Atlantis massif (Mid-Atlantic Ridge). These aromatic amino acids may have been formed through Friedel-Crafts reactions catalyzed by an iron-rich saponite clay during a late alteration stage of the massif serpentinites. Demonstrating the potential of fluid-rock interactions in the oceanic lithosphere to generate amino acids abiotically gives credence to the hydrothermal theory for the origin of**

[1]Institut de Physique du Globe de Paris, Sorbonne Paris Cité, Université Paris Diderot, CNRS, 1 rue Jussieu, 75238 Paris Cedex 05, France. [2]Synchrotron SOLEIL, L'Orme des Merisiers, Saint Aubin, BP 48, 91192 Gif-sur-Yvette Cedex, France. [3]Laboratoire de Géologie de Lyon: Terre, Planètes, Environnement, UMR5276, ENS-Université Lyon I, Campus de la Doua, bâtiment Géode, 2 rue Raphaël Dubois, 69622 Villeurbanne Cedex, France. [4]Institut de Chimie des Substances Naturelles, CNRS UPR2301, Université Paris-Sud, Université Paris-Saclay, avenue de la Terrasse, 91198 Gif-sur-Yvette, France. [5]Nazarbayev University, School of Mining and Geosciences, 53 Kabanbay Batyr avenue, 010000 Astana, Kazakhstan.

**life, and may shed light on ancient metabolisms and the functioning of the present-day deep biosphere.**

Abiotic synthesis of organic compounds by reduction of inorganic carbon species is thermodynamically favored by the production of molecular hydrogen ($H_2$), which accompanies serpentinization reactions[1]. In these hydration reactions, the production of $H_2$ results from the reduction of water coupled to the oxidation of the ferrous iron in olivine and pyroxene, the major rock-forming minerals of the upper mantle[1-2]. Therefore, hydrothermal areas where active serpentinization occurs are increasingly regarded as possible settings for the appearance of the first building blocks of life and the emergence of primordial metabolisms[3-4]. In that perspective, the discovery of the Lost City hydrothermal field hosted on the Atlantis Massif near the Mid-Atlantic Ridge (MAR)[5] deeply changed our vision of Earth habitability as it provides a modern example of $H_2$-rich alkaline fluids generated at moderate temperatures (50-150°C), *i.e.* the most favorable conditions for the appearance of life[6].

During the last two decades, experimental studies and thermodynamic calculations outlined the potential of serpentinization reactions to promote the abiotic formation of a diversity of organic compounds, including some of direct interest to prebiotic chemistry such as the protein-forming amino acids (Supplementary Table 1). However, reaction pathways for the abiotic formation of amino acids under hydrothermal conditions are still not well constrained, although several mechanisms have been proposed. Among the most commonly invoked reactions, the Strecker synthesis produces amino acids (mostly aliphatic) from the reaction of aldehydes or ketones with ammonia and cyanide. The overall reaction is thermodynamically

favored in hydrothermal environments and possibly catalyzed by metals and minerals (Supplementary Table 1).

Geochemical and isotopic evidence demonstrates abiotic synthesis of only a restricted number of low-molecular-weight organic compounds in hydrothermal systems associated with serpentinization on Earth. These compounds include mainly methane, short-chain alkanes and formate[7]. Although the presence of amino acids has been reported in hydrothermal vent fluids, with concentrations reaching several hundreds to thousands of nanomoles, these amino acids most likely derived from ecosystems hosted in the shallow oceanic crust[8]. Primordial amino acids and other nitrogen-bearing organic compounds have generally been considered as extraterrestrial in origin, and exogenously delivered to Earth by comets and asteroids[9]. These organic nitrogen compounds would be inherited from the aqueous alteration of the chondrite parent bodies or the asteroidal meteorites themselves, in a process resembling serpentinization as it occurs on Earth[10-11]. Although ref. (8) acknowledges that some of the amino acids detected at the Lost City hydrothermal field could have been synthesized abiotically, the possibility that the serpentinizing oceanic lithosphere could represent an efficient factory for nitrogen-bearing organic compounds has been poorly assessed until now. The current approaches are indeed mainly based on the analysis of fluids discharged at hydrothermal vents where, if abiotic synthesis would occur, products are likely too diluted to be distinguished from background biological contamination[8].

**Serpentinite-hosted amino acids**

Our study focuses on a deeply serpentinized harzburgite recovered by drilling in the Atlantis massif at a depth of 173.15 meters below sea floor (mbsf) during the IODP expedition 304 Leg

1309D[12]. The Atlantis massif is a tectonically-exhumed dome (~16 km across and rising 4,267 m above the seafloor) associated with an oceanic core complex located at the intersection between the MAR and the Atlantis transform fault (30°8'N-42°8'W). The sample was selected based on its elevated content in organic carbon determined by elemental analysis (*i.e.* 232 ppm)[13]. The high-temperature (300-350°C)[12] hydrated paragenesis resembles that usually found in serpentinized peridotites, with olivine being replaced by serpentine and magnetite exhibiting a characteristic mesh texture (Extended Data Fig. 1). Yellow to brownish phases are frequently found in the core of the mesh serpentine (Fig. 1a and Extended Data Fig. 1). These phases correspond to Fe-rich serpentine and Fe-rich saponite enriched in organic carbon (Fig. 2 and Extended Data Figs. 2 and 3f)[14-15]. They formed respectively during a second and third stage of hydrothermal alteration occurring at lower temperature (<200°C for Fe-rich serpentine[16] and <100-150°C for saponite[17]) at the expense of the first generation of serpentine and of the olivine kernels, some remnants of which can still be observed (Extended Data Fig. 1).

Synchrotron-coupled Deep-Ultra-Violet (S-DUV) microspectroscopy with excitation in the range 250-310 nm revealed an intense UV-autofluorescence (Fig. 1 and Extended Data Fig. 4) where Fe-rich saponite was present (Fig. 2 and Extended Data Figs. 2-3). Full-field imaging of the fluorescence collected in the 400-440 nm range following excitation at 275 nm showed a heterogeneous spatial distribution of the strongest fluorescence intensities forming a tortuous network within Fe-rich saponite (Fig. 1b). This is consistent with Scanning Electron Microscopy (SEM) observations highlighting variable content in the organic carbon trapped in this mineral phase (Figs. 2a-b). S-DUV autofluorescence was weaker in the Fe-rich serpentine compared to the Fe-rich saponite and nearly absent in the adjacent mesh serpentine (Fig. 1). The fluorescence signal collected between 300 and 550 nm after excitation at 275 nm was characterized by four

broad and overlapping bands respectively centered at 340±6, 358±3, 380±3 and 403±3 nm (Fig. 1 and Extended Data Fig. 4). These spectral features are indicative of the presence of tryptophan to which the band at 358 nm can be assigned, and of indole, skatole, and hydroxyanthranilic acid whose fluorescence spectra can be found in ref. (18). These three latter compounds may correspond to products of either natural[18] or UV-induced degradation[19] of tryptophan, although indole can also be an intermediate in the abiotic synthesis of tryptophan[20]. The four organic compounds were always spatially associated at comparable relative intensities (Extended Data Fig. 4). In contrast to the fluorescence emission observed upon excitation at 275 nm, which is close to the maximum absorption wavelength of tryptophan[21], excitations at wavelengths of 250 and 310 nm did not lead to any other endogenous fluorescence emission (Fig. 1c). Whereas protein-forming tryptophan in biological cells fluoresces at 335 nm after excitation at 275 nm and does not produce significant signals at higher wavelengths (Fig. 1c)[21], the UV-fluorescence emission value obtained here for tryptophan agrees with the maximum of fluorescence emission that arises when this amino acid is free (*i.e.* 360 nm)[21], the spectral shift being due to environment-related effects.

In agreement with S-DUV microspectroscopy, Time-of-Flight Secondary Ion Mass Spectrometry (TOF-SIMS) imaging recorded in Fe-rich saponite revealed a systematic presence of fragment ions characteristic of tryptophan (*e.g.* $C_9H_8N^+$; Figs. 3b-c and Extended Data Table 1)[22]. In addition to saponite/Fe-rich serpentine assemblages, tryptophan was also detected inside saponite close to olivine kernels, although more spatially restricted and at lower fluorescence intensities (Fig. 4). In all the areas where saponite and fragment ions characteristic of tryptophan were both detected, TOF-SIMS analysis did not provide any evidence for the presence of biomarkers, such as hopanoids, cholestane, pristane, squalane, lycopane or β-carotane[23-25], which

are constituents of marine dissolved organic carbon[13] or of deep microbial communities (Fig. 3d and Extended Data Fig. 6).

The presence of N-bearing organic compounds in the Fe-rich saponite was confirmed by Synchrotron-Fourier-Transform-Infrared microspectroscopy (S-FTIR) with vibrational modes attributable to pyrrole and aromatic rings (at 1380 $cm^{-1}$ and 1460-1465 $cm^{-1}$), α-amines (in the ranges 1460-1465 $cm^{-1}$ and 1550-1650 $cm^{-1}$) and carboxyl functional groups (at 1412 $cm^{-1}$ and 1728 $cm^{-1}$) (Extended Data Figs. 2b-c and Extended Data Table 2). The distribution of the absorption bands resembles that observed for tryptophan[26], although with higher relative proportions of primary amines and heterocycles and higher aliphaticity. Consequently, the broad absorption band between 1550 and 1650 $cm^{-1}$ likely represents multiple overlapping bands from different N-bearing heterocycles, as also observed by S-DUV microspectroscopy. Again, no absorption bands were detected between 1627 and 1670 $cm^{-1}$ where the characteristic amide I absorption band of protein secondary structures is observed[27].

**An abiotic origin for the amino acids**

The unique organic signatures derived from S-DUV, S-FTIR and TOF-SIMS measurements, all preferentially associated with the Fe-rich saponite, are clearly different from those obtained under comparable analytical conditions for microbial cells or biofilm-forming extracellular polymeric substances (Figs. 1c and 3; Extended Data Figs. 2b and 6). The presence of microbes or their remnants would have resulted in a spatially variable complex mixture of biopolymers, all carrying diverse functional groups[28]. In contrast, the organic material detected here corresponds to low-molecular-weight compounds with TOF-SIMS $m/z < 350$ (Fig. 3d and Extended Data Figs. 6). In addition, S-DUV, S-FTIR and TOF-SIMS analyses constantly display spectral

signatures that vary little from one micrometer to the other, all in favor of an abiotic origin for the tryptophan. In agreement with this hypothesis, as observed by Transmission Electron Microscopy (TEM), the Fe-rich saponite nanoporous network hosting the tryptophan signal is too tiny to host or have hosted prokaryotic cells of a few micrometers (Figs. 4d and 5a-b and Extended Data Figs. 3 and 5). The lack of amino acid characteristic signal in microfractures related to the Fe-rich saponite claims in favor of the endogenicity of the detected tryptophan.

At the nanoscale, the C-enriched Fe-rich saponite displayed highly-variable texture and porosity (Figs. 4d and 5a-b). At the interface between olivine crystals and mesh serpentine or Fe-rich serpentine, *i.e.* where organic compounds displayed weak UV-fluorescence and TOF-SIMS signals (Fig. 4), Fe-rich saponite lamellae are mainly subparallel although some sheet distortions are visible (Fig. 4d and Extended Data Fig. 5). Where tryptophan was found at higher concentrations in assemblages of Fe-rich saponite and Fe-rich serpentine (Figs. 1-3 and Extended Data Figs. 2-4), TEM showed the presence of packed saponite sheets in face-face mode or edge-face mode, forming a nanoporous house of cards structure (Figs. 5a-b). Such a state of structural disorder is supported by the lack of absorption at 3415 $cm^{-1}$ in the Fe-rich saponite S-FTIR spectra, a band that theoretically corresponds to interlamellar water[29]. Taken together, all these observations suggest the formation of a reactive organoclay[30] during the late stages of aqueous alteration of the Atlantis massif serpentinite.

**Abiotic Friedel-Crafts type synthesis**

Saponite, a tetrahedrally-charged trioctahedral smectite, is a well-known acid catalyst with high adsorption, swelling and cation exchange capacities[29]. These properties are widely used in the industry for organic synthesis or for the reduction of inorganic nitrogen species[29-30]. Some

varieties of smectite, including saponite, were shown to promote the abiotic synthesis of monocyclic as well as polycyclic aromatic hydrocarbons from methanol under hydrothermal conditions (*i.e.* 300°C, 100 MPa)[31]. Smectite properties make possible the formation of pillared structures out of their expandable silicate sheets by insertion, after exchange with interlayer water, of ionic compounds and/or organic moieties acting as pillars propping apart the clay sheets at increased interlayer distances (Fig. 5c), as observed by TEM (Fig. 4d). Further stacking and distortion of the clay lamellae creates a network of interconnected nanopores with increased surface area and reducing properties where organosynthesis can proceed and enhances interlayer expansion (Figs. 5a-b and d)[30].

In the general structure of saponite, the octahedral sites are usually occupied by $Mg^{2+}$ ions, while $Al^{3+}$ ions substitute for Si in the tetrahedral sites. In the iron-bearing variety, both $Fe^{2+}$ and $Fe^{3+}$ cations replace $Mg^{2+}$ and $Al^{3+}$ (Extended Data Tables 3 and 4), thus conserving the negative charge of the silicate sheets and hence the cation exchange capacities while maintaining the layered structure[32]. The presence of $Fe^{3+}$ ions in the tetrahedral sheets (Extended Data Table 4) also enhances surface acidity and therefore the sorption and catalysis properties of saponite[32]. The existence in the silicate sheet of Brønsted and Lewis acid sites to which aromatic and heteroatomic compounds may sorb is suggested by the multiple absorption bands observed between 1550 and 1650 $cm^{-1}$ on the Fe-rich saponite S-FTIR spectrum (Extended Data Fig. 2b)[29,33].

Due to their pillaring effect, enhanced sorption capacity and high reducible iron content, Fe-smectites have been shown to be the most efficient solid catalyst for Friedel-Crafts reactions[34]. Friedel-Crafts-type reactions are the method of choice in the industry for the alkylation of arenes and heteroarenes under the catalytic effect of Lewis or Brønsted acids, with

or without co-catalysts[35]. In the present case, Friedel-Crafts-type reactions may therefore represent an attractive explanation for the formation of aromatic amino acids such as tryptophan. In the commonly-considered Strecker synthesis[7], aliphatic amino acids are predominantly formed (Supplementary Table 1) and additional reaction steps are subsequently required to form aromatic amino acids. In contrast, starting from aromatic hydrocarbons or heteroaromatic compounds to which substituents are added, Friedel-Crafts reactions may offer a more direct route towards the formation of tryptophan at the acid sites of Fe-rich saponite, as demonstrated experimentally through asymmetric alkylation of indole with various catalysts[20]. Also in favor of such a hypothesis is the considerable thermodynamic potential for the hydrothermal synthesis of polycyclic aromatic hydrocarbons during serpentinization[36]. (Poly)aromatic hydrocarbons may hence be available as possible reactants in the shallow oceanic lithosphere.

We therefore propose that Friedel-Crafts reactions may be responsible for the formation of abiotic aromatic amino acids during the hydrothermal alteration of oceanic peridotites, this formation being catalyzed by Fe-rich saponite. Possible pathways could involve alkylation of indole with pyruvate followed by amination, the abiotic synthesis of pyruvate under hydrothermal conditions being demonstrated experimentally[37]. In addition, as shown in Extended Data Fig. 7 and Supplementary Information, chemical affinity calculations using concentrations reported for the Lost City hydrothermal fluid endmember suggest that the abiotic formation of indole, pyruvate and tryptophan from $HCO_3^-$, $H_2$, and $NH_3$ is thermodynamically favorable under the temperature, pH, and redox conditions prevailing in the Atlantis massif according to refs. (38-39) (*i.e.* 100°C, pH = 8.5, $a_{H_{2(aq)}} \sim 10^{-2}$ with $a_{H_{2(aq)}}$, the activity of aqueous hydrogen). The presence of $NH_3$ as the dominant form of nitrogen in the Atlantis massif is supported by additional thermodynamic calculations (Extended Data Fig. 8) and the general recognition that

crustal nitrogen-reduction reactions operate during hydrothermal circulation, turning oceanic nitrite and nitrate, and mantellic $N_2$ into stable $NH_3$ and $NH_4^+$, depending on pH[40-41].

## Implications

The results reported above clearly indicate that clay-forming hydrothermal alteration of oceanic rocks play a fundamental role in the synthesis and stabilization of such complex organic compounds as aromatic amino acids. This may have far reaching implications for the carbon and nitrogen cycles in the Earth system, as well as for the potential for prebiotic chemistry on Earth and the deep biosphere.

Although little is known about the concentration of inorganic nitrogen species in the Lost City hydrothermal fluids[8], our discovery first implies that these fluids transport sufficient nitrogen for the abiotic synthesis of N-bearing organic compounds. Second, our observations may also extend the ranges of depths and temperatures beyond those generally considered as compatible for the formation and preservation of organic molecules of prebiotic interest (*i.e.* in the deep subsurface *vs* in hydrothermal vents). In a reduced rocky environment isolated from the open ocean and atmosphere, sorptive mechanisms can additionally protect the clay-trapped amino acids from hydrolysis[42], as proposed for carbonaceous meteorites[43]. Further petrological, geochemical and thermodynamic investigations are however needed to better constrain the conditions under which the Fe-rich saponite was formed in the Atlantis massif, saponite precipitation occurring over a relatively large temperature range (*i.e.* 25-200ºC)[44].

Nonetheless, saponite constitutes the main product of the alteration of basalts and ultramafic rocks by silica-enriched hydrothermal fluids[44]. Fe-rich saponite with its capability to promote and preserve precursors of biopolymers, may have contributed to lay the foundations for

223 prebiotic synthesis when abundant ultramafic rocks formed the undifferentiated primeval
224 lithosphere covered by the large Hadean ocean[45]. Although the diversity of amino acids possibly
225 synthesized in such a context need to be further explored, the scheme proposed here offers a
226 powerful mechanism to drive the synthesis of prebiotic compounds under realistic Archaean
227 conditions. Concentration and some forms of condensation, polymerization and further chemical
228 evolution are possible in the chemically-reducing nanopores formed by the Fe-rich saponite
229 sheets acting as a confined microreactor (Fig. 5). While tryptophan may not have served as a first
230 protein building block[46], amino acids are also known to serve as biochemical precursors, deemed
231 to catalyze the synthesis of sugars, aldehydes and nucleotide intermediates[47]. If hyperalkaline
232 hydrothermal vent chimneys received a lot of attention for their vast network of
233 microcompartments walled by catalytic minerals, allowing the concentration of organic synthesis
234 products on the early Earth[3], Fe-rich saponite with its tiny protective niches offers comparable
235 attractiveness. Its ion exchange capability drives chemical gradients and non-equilibrium
236 conditions while the silicate layers may play the interface role of cell membranes[48].
237 Finally, the possibility of abiotically-formed amino acids in the recesses of the oceanic
238 lithosphere has also important consequences for ancestral metabolisms and microbial life
239 strategies in the present-day deep biosphere. Both are strongly linked to the nature of compounds
240 that can be used as carbon and energy sources. Enlarging with amino acids the range of possible
241 abiotic organic compounds formed in the terrestrial crust offers an additional opportunity for
242 (organo)heterotrophy to operate in these deep environments[49]. Anaerobic amino acid
243 fermentation, known as the Stickland reaction, involves amino acids, possibly of the same type,
244 serving both as electron donors and acceptors[50]. Stickland reaction is a typical pathway of
245 anaerobic bacteria belonging to the Firmicutes phylum, which can be found in serpentinization

environments where electron acceptors are lacking[49]. Whether abiotic amino acids may represent valuable substrates for the ecosystems inhabiting serpentinites, and whether they have shaped ancient microbial metabolisms or played a role in the emergence of a first form of biochemistry on Earth remains to be addressed. Nevertheless, the new formation pathway proposed here nurture the hydrothermal origin of life debate with an attractive alternative to the commonly considered Strecker and Fischer-Tropsch-type reactions.

**Online Content** Methods, along with any additional Extended Data display items, are available in the online version of the paper; references unique to these sections appear only in the online paper.

**Data Availability** The data supporting the findings of this study are available within the paper, its Extended Data and its Supplementary Information.


1. McCollom, T. M. & Seewald, J. S. Abiotic synthesis of organic compounds in deep-sea hydrothermal environments. *Chem. Rev.* **107**, 382-401 (2007).
2. Mével, C. Serpentinization of abyssal peridotites at mid-ocean ridges. *C. R. Geosci.* **335**, 825-852 (2003).
3. Martin, W., Baross, J., Kelley, D. & Russell, M. J. Hydrothermal vents and the origin of life. *Nat. Rev. Microbiol.* **6**, 805-814 (2008).
4. Sleep, N. H., Meibom, A., Fridriksson, Th., Coleman, R. G. & Bird, D. K. $H_2$-rich fluids from serpentinization: geochemical and biotic implications. *Proc. Natl. Acad. Sci. U.S.A.* **101**, 12818-12823 (2004).

5. Kelley, D. S. *et al.* An off-axis hydrothermal vent field near the Mid-Atlantic Ridge at 30° N. *Nature* **412**, 145-149 (2001).
6. Russell, M. J. The alkaline solution to the emergence of life: energy, entropy and early evolution. *Acta Biotheor.* **55**,133-179 (2007).
7. Konn, C., Charlou, J. L., Holm, N. G. & Mousis, O. The production of methane, hydrogen, and organic compounds in ultramafic-hosted hydrothermal vents of the Mid-Atlantic Ridge. *Astrobiology* **15**, 381-399 (2015).
8. Lang, S. Q., Früh-Green, G. L., Bernasconi, S. M. & Butterfield, D. A. Sources of organic nitrogen at the serpentinite-hosted Lost City hydrothermal field. *Geobiology* **11**, 154-169 (2013).
9. Pizzarello, S., Williams, L. B., Lehman, J., Holland, G. P. & Yarger, J. L. Abundant ammonia in primitive asteroids and the case for a possible exobiology. *Proc. Natl. Acad. Sci. U.S.A.* **108**, 4303-4306 (2011).
10. Elsila, J. E. *et al.* Meteoritic amino acids: diversity in compositions reflects parent body histories. *ACS Cent. Sci.* **2**, 370-379 (2016).
11. Elmaleh, A. *et al.* Formation and transformations of Fe-rich serpentines by asteroidal aqueous alteration processes: A nanoscale study of the Murray chondrite. *Geochim. Cosmochim. Acta* **158**, 162-178 (2015).
12. Blackman, D. K. *et al.* Drilling constraints on lithospheric accretion and evolution at Atlantis Massif, Mid-Atlantic Ridge 30° N. *J. Geophys. Res.* **116**, B07103 (2011).
13. Delacour, A., Früh-Green, G. L., Bernasconi, S. M., Schaeffer, P. & Kelley, D. S. Carbon geochemistry of serpentinites in the Lost City Hydrothermal System (30°N, MAR). *Geochim. Cosmochim. Acta* **72**, 3681-3702 (2008).

14. Bisio, C. *et al.* Understanding physico-chemical properties of saponite synthetic clays. *Microporous Mesoporous Mater.* **107**, 90-101 (2008).
15. Pisapia, C., Jamme, F., Duponchel, L. & Ménez, B. Tracking hidden organic carbon in rocks using chemometrics and hyperspectral imaging. *Sci. Rep.* **8**, 2396 (2018).
16. Klein, F. *et al.* Magnetite in seafloor serpentinites- Some like it hot. *Geology* **42**, 135-138 (2014).
17. Nozaka, T., Fryer, P. & Andreani, M. Formation of clay minerals and exhumation of lower-crustal rocks at Atlantis Massif, Mid-Atlantic Ridge. *Geochem. Geophys. Geosyst.* **9**, Q11005 (2008).
18. Determann, S., Lobbes, J. M., Reuter, R. & Rullkötter, J. Ultraviolet fluorescence excitation and emission spectroscopy of marine algae and bacteria. *Mar. Chem.* **62**, 137-156 (1998).
19. Kumamoto, Y., Fujita, K., Smith, N. I. & Kawata, S. Deep-UV biological imaging by lanthanide ion molecular protection. *Biomed. Opt. Express* **7**, 158-170 (2016).
20. Pavlov, N. *et al.* Asymmetric synthesis of $\beta^2$-tryptophan analogues via Friedel-Crafts alkylation of indoles with a chiral nitroacrylate. *J. Org. Chem.* **76**, 6116-6124 (2011).
21. Jamme, F. *et al.* Synchrotron UV fluorescence microscopy uncovers new probes in cells and tissues. *Microsc. Microanal.* **16**, 507-514 (2010).
22. Sanni, O. D., Wagner, M. S., Briggs, D., Castner, D. G. & Vickerman, J. C. Classification of adsorbed protein static ToF-SIMS spectra by principal component analysis and neural networks. *Surf. Interface Anal.* **33**, 715-728 (2002).
23. Steele, A., Toporski, J. K. W., Avci, R., Guidry, S. & McKay, D. S. Time of flight secondary ion mass spectrometry (ToFSIMS) of a number of hopanoids. *Org. Geochem.* **32**, 905-911 (2001).

24. Toporski, J. K. W. & Steele, A. Characterization of purified biomarker compounds using time of flight-secondary ion mass spectrometry (ToF-SIMS). *Org. Geochem.* **35**, 793-811 (2004).
25. Siljeström, S. *et al.* Detection of organic biomarkers in crude oils using ToF-SIMS. *Org. Geochem.* **40**, 135-143 (2009).
26. http://webbook.nist.gov/cgi/cbook.cgi?ID=C73223&Type=IR-SPEC&Index=1
27. Chiriboga, L. *et al.* Infrared spectroscopy of human tissue. I. Differentiation and maturation of epithelial cells in the human cervix. *Biospectroscopy* **4**, 47-53 (1998).
28. Ménez, B., Pasini, V. & Brunelli, D. Life in the hydrated suboceanic mantle. *Nat. Geosci.* **5**, 133-137 (2012).
29. Kooli, F. & Jones, W. Characterization and catalytic properties of a saponite clay modified by acid activation. *Clay Miner.* **32**, 633-643 (1997).
30. Molina, C. B., Casas, J. A., Pizarro, A. H. & Rodriguez, J. J. Pillared clays as green chemistry catalysts: Application to wastewater treatment, in *Clay: Types, Properties and Uses* (eds Humphrey, J. P. & Boyd, D. E.). Nova Science Publisher, New York, USA, 435-474 (2011).
31. Williams, L. B. *et al.* Birth of biomolecules from the warm wet sheets of clays near spreading centers, in *Earliest Life on Earth: Habitats, Environments and Methods of Detection* (eds Golding, S. D. & Glikson, M.). Springer, Amsterdam, the Netherlands, 79-112 (2010).
32. Meunier, A., Petit, S., Cockell, C. S., El Albani, A. & Beaufort, D. The Fe-rich clay microsystems in basalt-komatiite lavas: importance of Fe-smectites for pre-biotic molecule catalysis during the Hadean eon. *Origins Life Evol. Biosphere* **40**, 253-273 (2010).

33. Belver, C., Bañares-Muñoz, M. A. & Vicente, M. A. Fe-saponite pillared and impregnated catalysts I. Preparation and characterization. *Appl. Catal. B* **50**, 101-112 (2004).
34. Choudary, B. M., Kantam, M. L., Sateesh, M., Rao, K. K. & Santhi, P. L. Iron pillared clays - efficient catalysts for Friedel-Crafts reactions. *Appl. Catal. A* **149**, 257-264 (1997).
35. Rueping, M. & Nachtsheim, B. J. A review of new developments in the Friedel-Crafts alkylation - From green chemistry to asymmetric catalysis. *Beilstein J. Org. Chem.* **6**, No. 6 (2010).
36. Milesi, V., McCollom, T. M. & Guyot, F. Thermodynamic constraints on the formation of condensed carbon from serpentinization fluids. *Geochim. Cosmochim. Acta* **189**, 391-403 (2016).
37. Cody, G. D. *et al.* Primordial carbonylated iron-sulfur compounds and the synthesis of pyruvate. *Science* **289**, 1337-1340 (2000).
38. Seyfried, W. E. Jr., Pester, N. J., Tutolo, B. M. & Ding, K. The Lost City hydrothermal system: Constraints imposed by vent fluid chemistry and reaction path models on subseafloor heat and mass transfer processes. *Geochim. Cosmochim. Acta* **163**, 59-79 (2015).
39. Proskurowski, G., Lilley, M. D., Kelley, D. S. & Olson, E. J. Low temperature volatile production at the Lost City Hydrothermal Field, evidence from a hydrogen stable isotope geothermometer. *Chem. Geol.* **229**, 331-343 (2006).
40. Brandes, J. *et al.* Abiotic nitrogen reduction on the early Earth. *Nature* **395**, 365-368 (1998).
41. Schoonen, M. A. & Xu, Y. Nitrogen reduction under hydrothermal vent conditions: implications for the prebiotic synthesis of C-H-O-N compounds. *Astrobiology* **1**, 133-142 (2001).

42. Salmon, V., Derenne, S., Lallier-Vergès, E., Largeau, C. & Beaudoin, B. Protection of organic matter by mineral matrix in a Cenomanian black shale. *Org. Geochem.* **31**, 463-474 (2000).

43. Pearson, V. K. *et al.* Clay mineral-organic matter relationships in the early solar system. *Meteorit. Planet. Sci.* **37**, 1829-1833 (2002).

44. Manuella, F. C., Carbone, S. & Barreca, G. Origin of saponite-rich clays in a fossil serpentinite-hosted hydrothermal system in the crustal basement of the Hyblean Plateau (Sicily, Italy). *Clays Clay Miner*. **60**, 18-31 (2012).

45. Arndt, N. T. & Nisbet, E. G. Processes on the young Earth and the habitats of early life. *Annu. Rev. Earth Planet. Sci.* **40**, 521-549 (2012).

46. Granold, M., Hajieva, P., Toşa, M. I., Irimie, F.-D. & Moosmann, B. Modern diversification of the amino acid repertoire driven by oxygen. *Proc. Natl. Acad. Sci. U. S. A.* **115**, 41-46 (2018).

47. Ruiz-Mirazo, K., Briones, C. & de la Escosura, A. Prebiotic systems chemistry: New perspectives for the origins of life. *Chem. Rev.* **114**, 285-366 (2014).

48. Russell, M. J., Daniel, R. M., Hall, A. J. & Sherringham, J. A. A hydrothermally precipitated catalytic iron sulphide membrane as a first step toward life. *J. Mol. Evol.* **39**, 231-243 (1994).

49. Schrenk, M. O., Brazelton, W. J. & Lang, S. Q. Serpentinization, carbon and deep life, in *Carbon in Earth* (eds Hazen, R. M., Jones, A. P. & Baross J. A.). Mineralogical Society of America, Chantilly, USA, Reviews in Mineralogy & Geochemistry, vol. **75**, 575-606 (2013).

50. Barker, H. A. Fermentation of nitrogenous compounds, in *The Bacteria. A Treatise on Structure and Function* (eds Gunsalus, I. C. & Stanier, R. Y.). Academic Press, Cambridge, Massachusetts, 151-207 (1961).

**Supplementary Information** including Methods is linked to the online version of the paper at www.nature.com/nature.

**Acknowledgments** We thank B. Van de Moortèle for the FIB ultrathin sections, O. Boudouma for assistance during SEM experiments along with V. Pasini and D. Brunelli for discussion and help during S-FTIR experiments and M. Chaussidon for comments on the manuscript. We acknowledge the IODP program (https://www.iodp.org/) and SOLEIL synchrotron for granted access to DISCO and SMIS beamlines (proposals 20110217, 20110833, 99120080, 20120659 and 20140590). This research was supported by the Deep Carbon Observatory awarded by Alfred P. Sloan Foundation, the deepOASES ANR project (ANR-14-CE01-0008) and the French CNRS (Mission pour l'Interdisciplinarité, Défi Origines 2018). This is IPGP contribution n° XXX.

**Author Contributions** B.M., M.A., C.P. conceived the research. B.M., C.P., F.J., M.R., Q.P.V., A.B., M.A., and P.D. performed the experiments. L.R. performed the thermodynamic calculations. B.M. wrote the manuscript. All authors contributed to the interpretation of the data and commented on the drafts of the manuscript.

**Author Information** Reprints and permissions information is available at www.nature.com/reprints. The authors declare no competing financial interests. Readers are welcome to comment on the online version of the paper. Publisher's note: Springer Nature remains neutral with regard to jurisdictional claims in published maps and institutional

affiliations. Correspondence and requests for materials should be addressed to B.M. (menez@ipgp.fr) or M.A. (muriel.andreani@univ-lyon1.fr).

## Figure Captions

**Figure 1 | Endogenous UV-autofluorescence locally revealed by S-DUV imaging of a highly altered mantle rock recovered at 173.15 mbsf from IODP Hole 304-1309D[12]. UV-fluorescence emerged from heteroatomic aromatic compounds shown to be spatially restricted to a Fe-rich clay in which they are heterogeneously distributed**. **a**, Optical image showing yellow to brownish phases identified as Fe-rich serpentine (Fe-Srp) and Fe-rich saponite (Sap), hosted in a serpentinized harzburgite with olivine being replaced by magnetite (Mag) and serpentine exhibiting a characteristic mesh texture (mesh Srp); the green arrow indicates sample orientation. The light green square in **a** depicts the location of the full field S-DUV image displayed in **b** and collected between 400 and 440 nm using excitation ($\lambda_{exc}$) at 275 nm. "a.u.", arbitrary unit. **c**, Fluorescence emission spectra collected with excitation wavelengths of 250, 275 and 310 nm at the location shown by an asterisk in **b**. The spectra collected at 250 and 310 nm do not show any significant UV-autofluorescence signal whereas the spectrum at 275 nm displays fluorescence characteristic of indole at 340±6 nm, tryptophan at 358±3 nm, skatole at 380±3 nm, and hydroxyanthranilic acid at 403±3 nm[18]. Also shown are a fluorescence emission spectrum collected at 275 nm in the Fe-rich serpentine and the typical emission spectrum of a biological cell showing fluorescence maximum emission, mainly arising from protein-forming tryptophan, shifted to 335 nm[21]. The orange area in **c** represents the fluorescence detection range used in **b**. The blue box in **a** indicates the location where complementary S-FTIR measurements were performed (Extended Data Fig. 2).

**Figure 2 | SEM images of the Fe-rich saponite enriched in organic carbon. a-b**, SEM-BSE images collected at 15 kV on the mineral assemblage displayed in Figs. 1 and 3 and Extended Data Fig. 1a with **b** being a close up view of the area indicated by the green box in **a**. The green arrow indicates sample orientation; the orange dashed line and the associated arrow respectively provide location and front face of the FIB foil milled for TEM observations (Figs. 5a-b and Extended Data Fig. 3). Textures and differences in grey levels resulting from chemical contrasts allow recognizing each mineral phase previously characterized by S-FTIR and electron microprobe analysis, namely mesh serpentine (mesh Srp), Fe-rich serpentine (Fe-Srp) and Fe-rich saponite (Sap). In particular, the characteristic platelets of saponite[14] are well recognizable in the SEM-SE image shown in **c** and collected at 3 kV accelerating voltage (location shown with an asterisk in **a**); Fe-rich saponite presents distinct grey levels in **a** and **b** that relate to its variable content in organic carbon, hence darkening its aspect when carbon is abundant.

**Figure 3 | The presence of tryptophan in the Fe-rich saponite was confirmed by TOF-SIMS imaging with the colocalized collection of its characteristic fragment ions** (Extended Data Table 1). **a**, TOF-SIMS ion image of mineral-derived $Fe^+$ showing location of analysis with respect to the mesh for the area displayed in Fig. 1a. The green arrow indicates sample orientation. "TC", total count. **b**, Molecular ion image (binning of 4) of the $C_9H_8N^+$ fragment ion at *m/z* 130.06 corresponding to the ion peak shown in **c**, which is characteristic of tryptophan[22]. It reveals cluster-like accumulations within the Fe-rich saponite. **d**, TOF-SIMS spectrum (*m/z* 200-600) reconstructed from the region displaying the highest count rates in **b**. It provides evidence for the absence of common biomarkers[23-25]. Detailed spectra are provided in Extended Data Figs. 6a-n.

**Figure 4 | Systematic association of Fe-rich saponite with tryptophan. a**, Optical view of an olivine (Ol) kernel in the mesh serpentine (mesh Srp) also shown in Extended Data Fig. 1b. The green square indicates the position of the associated SEM-BSE images shown in **b** and **c** and collected at 15 kV. **c**, Close up view of the area represented by the green box in **b**. The orange dashed line and associated arrow in **b** respectively provide location and front face of the FIB foil (Extended Data Fig. 5) milled for the TEM observations displayed in **d**. Textures and chemical contrasts allow recognizing each mineral phase previously characterized by S-FTIR and electron microprobe analysis, namely magnetite (Mag), Ol, mesh Srp, Fe-rich serpentine (Fe-Srp) and Fe-rich saponite (Sap). **d**, TEM image showing the Fe-rich saponite layers to appear perpendicular to the interface between the olivine kernel and the mesh serpentine with lizardite crystallites appearing in black. The Fe-rich saponite lamellae are mainly subparallel although some sheet distortions are visible. **e**, Associated S-DUV full field fluorescence images collected after excitation ($\lambda_{exc}$) at 275 nm in the range 327-353, 370-410 and 412-438 nm. They show for all these wavelengths, UV autofluorescence emission at the interface between olivine crystal and serpentine where the Fe-rich saponite is located. **f**, TOF-SIMS ion image collected in the 500×500 µm² area displayed in **a** and showing the distribution of the characteristic fragment ions of tryptophan[22] (Extended Data Table 1), hence confirming its presence close to the olivine kernel. Evidence for the absence of common biomarkers[23-25] can be found in the detailed spectra provided in Extended Data Figs. 6o-v. The green arrows provide sample orientation.

**Figure 5 | Fe-rich saponite played the role of a catalyzing pillared-clay for the abiotic synthesis of tryptophan. a-b**, TEM images collected on the ultrathin foil milled by FIB in the

area shown in Figs. 1-3 and Extended Data Figs. 2-4. The saponite (Sap) interfacing Fe-rich or mesh-serpentines shows the presence of aggregates formed by packing of sheets opening nanopores and suggests the occurrence of pillaring processes and a high reactivity of the clay. **c**, Clay minerals possess negatively-charged silicates layers with cations in the interlayer space to balance the charge. They all together allow sorption and exchanges of ions or organic moieties to occur during water-clay interactions, hence propping apart clay layers at increased interlayer distances, *i.e.* packing in face-face mode. **d**, Packing in face-face, edge-edge or edge-face mode resulting in a house of card structure recognizable in **a** and **b**. The nanoporous structure represents microreactors for the formation of tryptophan at the acid sites of the Fe-rich saponite.

**Online-only Methods (currently included in the Supplementary Information)**

# SUPPLEMENTARY INFORMATION

**TABLE OF CONTENTS**



## METHODS

**Sample preparation.** Drilled rock samples were sawed with sterile ultrapure water in order to extract the inner core, free of possible post-sampling contamination. The saw was previously treated with 5% sodium hypochlorite, then rinsed twice with sterile ultrapure water. The inner core was then manipulated using clean pliers, thinned and polished manually on both faces (down to a thickness of tens of micrometers) with pure ethanol using silicon carbide polishing disks without any use of resin or glue. Samples were then sequentially analyzed using, by order of potential beam-induced damages and sample preparation constraints (*e.g.* metallic coating or sample milling), Synchrotron-Fourier-Transform-Infra-Red microscopy (S-FTIR), Synchrotron-coupled Deep-Ultra-Violet (S-DUV) microspectroscopy, Time-of-Flight Secondary Ion Mass Spectrometry (TOF-SIMS) imaging, Scanning Electron Microscopy (SEM), and Transmission Electron Microscopy (TEM).

**Synchrotron-Fourier-Transform-Infrared microspectroscopy.** S-FTIR hyperspectral imaging was performed at the SMIS beamline (SOLEIL synchrotron radiation facility, Saint Aubin, France)[51] by taking advantage of the brightness of the bending magnet radiation and of the confocal geometry of the microscope objective[52]. The sensitivity of infrared microspectroscopy is on average $10^{-4}$ M ($10^{-12}$ g of molecules)[51]. Data were acquired in transmission mode with a Nicplan microscope coupled to a Magna 550 FT-IR spectrometer (Thermo-Nicolet). The confocal aperture was set at 5×5 µm² using a 32× infinity corrected Schwarzschild objective with a numerical aperture of 0.65 (Nicolet Reflachromat) and a matching 10× condenser. The microscope is equipped with a motorized sample stage (repeatability 1 µm) and a liquid nitrogen cooled mercury cadmium telluride detector (MCT-A; detector element size 250 µm). The sample was deposited on a $CaF_2$ window without any treatment. Hyperspectral data cubes in which pixels correspond to individual S-FTIR spectra were collected in the 4000-800 $cm^{-1}$ mid-infrared range using a step size of 5 µm. Acquisitions were carried out using 50 accumulations per spectrum/pixel with a spectral resolution set at 4 $cm^{-1}$. Spectrum analyses were first performed using OMNIC™ software (Thermo Fisher Scientific) to obtain distribution maps of the aliphatic

$CH_2/CH_3$ stretching band area between 2800-3000 $cm^{-1}$ and then using an approach combining Principal Component Analysis (PCA) and Multivariate Curve Resolution - Alternating Least Squares (MCR-ALS) implemented on the Matlab® software and the PLS toolbox (Eigenvector Research Inc.)[15].

**Synchrotron-coupled Deep-Ultra-Violet microspectroscopy.** S-DUV microspectroscopy allows imaging with a nanomolar sensitivity of aromatic, phenolic or unsaturated compounds without any external fluorescent probes[21]. Fluorescence imaging was carried out at the DISCO beamline (SOLEIL synchrotron radiation facility, Saint Aubin, France) where two complementary full UV compatible microscopes are coupled to the monochromatized synchrotron radiation continuously emitted from a bending magnet, which allows fluorescence excitation down to 180 nm (from 250 to 310 nm in the present study) at a submicrometric spatial resolution[53]. The use of a synchrotron light as a UV source allows to precisely tune the excitation light to the absorption of endogenous fluorochromes. Both microscopes, equipped with motorized sample stages (repeatability µm), were used with a Zeiss Ultrafluar 40× (glycerine immersion) objective. The sample was deposited on a quartz window without any treatment. In order to localize fluorescent areas within serpentinites, a full field Zeiss Axio Observer Z-1 inverted microscope was first used. The fluorescent signal was collected by a PIXIS 1024 BUV camera (Princeton Instruments) with bandpass filters at 327-353, 370-410, 412-438 and 400-440 nm (Semrock) and associated integration times of 120 s. Images were analyzed using the Fiji software[54] and stitched by linear blending[55]. Microspectrofluorescence emission spectra in the range 285-550 nm were thereafter collected with a 70% C Peltier-cooled iDus CCD detector (Andor) of 1024×256 pixels with a 26×26µm pixel size on selected areas using a spectral Olympus IX71 inverted microscope. Hyperspectral data cubes in which pixels correspond to individual fluorescence spectra were collected on areas up to 100×80 $\mu m^2$ in size with a 2 to 3 µm step size and 20 to 40 s acquisition time per spectrum/pixel. With the exception of manual removal of spikes coming from cosmic rays, no filtering or treatment of the autofluorescence spectra was conducted. Deconvoluted images of each individual fluorescent component were then produced with the Labspec software (Jobin-Yvon, France) using Gaussian functions and 10 iterations.

**Time-of-Flight Secondary Ion Mass Spectrometry imaging.** TOF-SIMS imaging allows to simultaneously detect inorganic and organic molecules on solid surfaces without extraction, chemical preparation or derivatization. Experiments were conducted using a TOF-SIMS IV reflectron-type mass spectrometer (IONTOF GmbH) located at the Institut de Chimie des Substances Naturelles (CNRS, Gif-sur-Yvette, France)[56]. The instrument is equipped with a bismuth liquid metal ion gun delivering a pulsed $Bi_3^+$ cluster ion beam. 25 keV primary ions impacted the sample at an incidence angle of 45° and a pulsed current of 0.1 pA. Emitted secondary ions were accelerated to 2 keV (2 kVextraction) toward a field-free region and a single stage reflectron (first-order compensation). Secondary ions ejected from the few upper monolayers of the sample surface were post-accelerated to 10 keV before reaching the detector made of a micro-channel plate, a scintillator and a photomultiplier. The ion column focusing mode ensured a spatial resolution of 2-5 µm and a mass resolution of 5000 (full width half-maximum) at *m/z* 500. A low-energy (~20 eV) electron flood gun was used between two successive primary ion pulses for charge compensation with minimum damage on the sample surface. An optical camera located in the sample vacuum chamber aided location of the samples, which were deposited on the sample holder without any treatment or adhesive. Ion images in both negative and positive polarities were acquired in a raster pattern on areas of 500×500 $\mu m^2$

and 256×256 pixels giving a pixel size of 1.95×1.95 µm². The images were recorded with a primary ion fluence of $3.44 \cdot \times 10^{11}$ ions·cm$^{-2}$ (400 scans with cycle time of 100 µs). The accumulated primary ion dose never exceeded $10^{12}$ ions·cm$^{-2}$, which is below the static limit for organic molecules[57]. Data acquisition and processing were done using the SurfaceLab 6 software (IONTOF GmbH). Spectra from the total analysis area or from selected regions of interest were extracted. Internal mass calibration was performed using the low mass fragment ion signals of $H^+$, $H_2^+$, $H_3^+$, $C^+$, $CH_3^+$, and $C_2H_3^+$ for the positive ion mode and $C^-$, $CH^-$, $CH_2^-$, $C_2^-$, $C_3^-$, and $C_4H^-$ for the negative ion mode. Assignments of ion peaks were made according to the instrument resolution, accuracy and the valence rule. The presence of tryptophan was investigated through the identification and assignment of all required fragment ions that are characteristic of this amino acid[58-60]. The absence of interferences was carefully checked for each assigned peak and mass deviations relatively to the theoretical *m/z* values were calculated. They all fall within admitted values for TOF-SIMS analyses (Extended Data Table 1). Image reconstruction for selected fragment ions was carried out by integrating signal intensities at given *m/z* values across the data set.

**Scanning Electron Microscopy.** SEM was performed at the Service Commun de Microscopie Electronique à Balayage (UPMC, Paris, France) on Au-coated samples with a Zeiss SUPRA 55 VP field emission microscope operating at 3 to 15kV accelerating voltage at respectively low and high currents (from 10 pA up to 1 nA). Images were collected using secondary electron (SE) detectors (Everhart-Thornley and InLens for high and low voltage mode, respectively) and a backscattered electron (BSE) detector (AsB). Images were further processed with the ImageJ software[61] for contrast and brightness adjustment.

**Focused Ion Beam (FIB) milling and Transmission Electron Microscopy**. As TEM requires samples to be electron transparent, ultrathin foils (thickness < 100 nm) were milled using a Zeiss NVision 40 cross beam microscope (CLYM, University of Lyon, France) which combines a high resolution field emission SEM with a Seiko FIB column. The 10-15 nm thick Au layer previously deposited for SEM observations prevented from amorphization of the subsurface. Additionally, before excavation, milled volumes were protected by a FIB-induced 1-2 µm thick carbon coating (Extended Data Figs. 3a-c and 5a-c) using a $Ga^+$ beam, emitted by a Ga liquid metal ion source operating at 30 kV accelerating voltage. To allow cross-sectional observations at depth (Extended Data Figs. 3c-e and 5c-d), excavations were first made on one side of the TEM foil location using ion beam current of decreasing intensities (13, 6.5, 3 nA and 700 pA). Cross-sectional images were collected at 5 kV using a Secondary Electrons Secondary Ions (SESI) detector and InLens detector for high and low voltage mode, respectively, and at 1.25 kV using an Energy Selective Backscattered BSE detector. Elemental analyses were carried out with an Oxford Instrument Energy Dispersive X-ray Spectrometer (EDS) (X-max 50 mm$^2$ silicon drift detector). TEM sections were then extracted from the bulk sample following excavation of its second side once a thickness of ~1-2 µm was reached. TEM sections were then fixed by C ion beam deposition on a half copper TEM grid. Further thinning of the TEM foil to few tens of nanometers was obtained with a glancing angle beam at low ion beam current (from 700 pA down to 50 pA at 30 kV). They were finally cleaned for traces of Ga ion implantation by a milling at 2 kV and 50 pA during 3-5 min on each side. TEM observations were then carried out with a TOPCON operating at 200 kV (CLYM, University of Lyon, France). Images, further processed with ImageJ software[61] for contrast and brightness adjustment, have been collected at a nanometric spatial resolution with a CCD Camera.

**Thermodynamic constraints on the abiotic synthesis of tryptophan at Lost City.** In order to evaluate the extent to which the temperature-pressure-composition conditions prevailing in the Lost City hydrothermal system are conducive to the abiotic synthesis of tryptophan and some of its possible precursors (indole and pyruvate) (Extended Data Fig. 7), the chemical affinities $A_r$ of their formation reactions were computed at 100°C from the relation

$$A_r = RT \ln(K_r/Q_r)$$

where $R$ and $T$ stands for the gas constant and absolute temperature, respectively, $Q_r$ is the reaction quotient, and $K_r$ is the thermodynamic equilibrium constant. The reaction quotient is calculated from the relation

$$Q_r = \prod_i a_i^{n_{i,r}}$$

where $a_i$ represents the activity of the $i^{\text{th}}$ species involved in the $r^{\text{th}}$ reaction, and $n_{i,r}$ is the stoichiometric coefficient of the species in the reaction. Note that the chemical affinities computed below are mathematically equivalent to the opposite of the overall Gibbs energies $\Delta G_r$ computed by ref. (62) for the abiotic synthesis of amino acids in accord with

$$\Delta G_r = \Delta G_r^\circ + RT \ln Q_r$$

where $\Delta G_r^\circ$ is the standard Gibbs energy of the abiotic synthesis reaction.

In the absence of Helgeson-Kirkham-Flowers (HKF) parameters for aqueous indole and pyruvate, the values of the equilibrium constants at 100°C were estimated using the van´t Hoff equation

$$\log K_{373.15\text{K}} = \log K_{298.15\text{K}} + \frac{\Delta H_r^\circ}{RT}\left(\frac{1}{373.15} - \frac{1}{298.15}\right)$$

where $\Delta H_r^\circ$ is the standard enthalpy of the reaction at 298.15 K. The equilibrium constants at 25°C and 100°C have been carried out using standard Gibbs energies and enthalpies of formation taken from refs. (63-64) for the aqueous inorganic species and from ref. (65) for aqueous tryptophan, indole and pyruvate.

Assuming a pH = 8.5 for a hypothetical Lost City fluid cooled to 100°C during its ascent towards the seafloor[38], the predominant inorganic carbon and nitrogen species are $HCO_3^-$ and $NH_{3(aq)}$ (Extended Data Fig. 8). Accordingly, the abiotic synthesis reactions have been written as

$$11\ HCO_3^- + 2\ NH_{3(aq)} + 23\ H_{2(aq)} + 11\ H^+ = C_{11}H_{12}N_2O_{2(aq)} + 20\ H_2O_{(l)}$$
(tryptophan)

$$8\ HCO_3^- + NH_{3(aq)} + 18\ H_{2(aq)} + 8\ H^+ = C_8H_7N_{(aq)} + 16\ H_2O_{(l)}$$
(indole)

and

$$3\ HCO_3^- + 5\ H_{2(aq)} + 2\ H^+ = C_3H_3O_3^- + 6\ H_2O_{(l)}$$
(pyruvate)

The reaction quotients were evaluated with activities for the aqueous species which approximate the concentrations reported for the Lost City hydrothermal fluids, *i.e.* $a_{CO_{2(aq)}} = 10^{-2.54}$ [66], $a_{H_{2(aq)}} \sim 10^{-2}$ [39], and $a_{NH_{3(aq)}} \sim 10^{-6}$ [8]. Nanomolar concentrations have been assumed for the organic compounds.

The chemical affinities calculated for the abiotic synthesis of tryptophan, indole, and pyruvate are respectively 134.5 kJ·mol$^{-1}$, 193.48 kJ·mol$^{-1}$ and 43.07 kJ·mol$^{-1}$. The chemical affinity for the synthesis of tryptophan is significantly more favorable than that calculated by ref. (62) because of the higher concentration of $H_2$ in the Lost City fluids. The dependence of the chemical affinities of the reactions on the activity of aqueous $H_2$ can be deduced from Extended

Data Fig. 7. It can be seen that the abiotic synthesis of tryptophan becomes favorable only for $H_2$ concentrations above ~ $10^{-2.8}$ *m*.

**Supplemental References**


51. Dumas, P. *et al.* Synchrotron infrared microscopy at the French Synchrotron Facility SOLEIL. *Infrared Phys. Techn.* **49**, 152-160 (2006).

52. Jamme, F., Lagarde, B., Giuliani, A., Garcia, G. A. & Mercury, L. Synchrotron infrared confocal microscope: Application to infrared 3D spectral imaging. *J. Phys.: Conf. Ser.* **425**, 142002 (2013).

53. Giuliani, A. *et al.* DISCO: a low-energy multipurpose beamline at synchrotron SOLEIL. *J. Synchrotron Radiat.* **16**, 835-841 (2009).

54. Schindelin, J. *et al.* Fiji: an open-source platform for biological-image analysis. *Nat. Methods* **9**, 676-682 (2012).

55. Preibisch, S., Saalfeld, S. & Tomancak, P. Globally optimal stitching of tiled 3D microscopic image acquisitions. *Bioinformatics* **25**, 1463-1465 (2009).

56. Brunelle, A., Touboul, D. & Laprévote, O. Biological tissue imaging with time-of-flight secondary ion mass spectrometry and cluster ion sources. *J. Mass Spectrom.* **40**, 985-999 (2005).

57. Touboul, D., Kollmer, F., Niehuis, E., Brunelle, A. & Laprévote, O. Improvement of biological time-of-flight-secondary ion mass spectrometry imaging with a bismuth cluster ion source. *J. Am. Soc. Mass Spectrom.* **16**, 1608-1618 (2005).

58. Mazel, V. *et al.* Identification of ritual blood in African artifacts using TOF-SIMS and synchrotron radiation microspectroscopies. *Anal. Chem.* **79**, 9253-9260 (2007).

59. Cersoy, S., Richardin, P., Walter, P. & Brunelle, A. Cluster TOF-SIMS imaging of human skin remains: analysis of a South-Andean mummy sample. *Mass Spectrom.* **47**, 338-346 (2012).

60. Farre, B. *et al.* Shell layers of the black-lip pearl oyster *Pinctada margaritifera*: matching microstructure and composition. *Comp. Biochem. Physiol. B* **159**, 131-139 (2011).

61. Schneider, C. A., Rasband, W. S. & Eliceiri, K. W. NIH Image to ImageJ: 25 years of image analysis. *Nat. Methods* **9**, 671-675 (2012).

62. Amend, J. P. & Shock, E. L. Energetics of amino acid synthesis in hydrothermal ecosystems. *Science* **281**, 1659-1662 (1998).

63. Shock, E. L. & Helgeson, H. C. Calculation of the thermodynamic and transport properties of aqueous species at high pressures and temperatures: Correlation algorithms for ionic species and equation of state predictions to 5 kb and 1000°C. *Geochim. Cosmochim. Acta* **52**, 2009-2036 (1988).

64. Shock, E. L., Helgeson, H. C. & Sverjensky, D. A. Calculation of the thermodynamic and transport properties of aqueous species at high pressures and temperatures: Standard partial molal properties of inorganic neutral species. *Geochim. Cosmochim. Acta* **53**, 2157-2183 (1989).

65. Tewari, Y. B. & Goldberg, R. N. An equilibrium and calorimetric investigation of the hydrolysis of L-tryptophan to (indole + pyruvate + ammonia). *J. Solution Chem.* **23**, 167-184 (1994).

66. Proskurowski, G. *et al.* Abiogenic hydrocarbon production at Lost City hydrothermal field. *Science* **319**, 604-607 (2008).

67. Aubrey, A., Cleaves, H. & Bada, J. The role of submarine hydrothermal systems in the synthesis of amino acids. *Origins Life Evol. Biosphere* **39**, 91-108 (2009).

68. Schulte, M. & Shock, E. Thermodynamics of Strecker synthesis in hydrothermal systems. *Origins Life Evol. Biosphere* **25**, 161-173 (1995).

69. Lowe, C. U., Markham, R. & Rees, M. W. Synthesis of complex organic compounds from stable precursors - formation of amino acids, amino acid polymers, fatty acids and purines from ammonium cyanide. *Nature* **199**, 219-220 (1963).

70. Wolman, Y., Miller, S. L., Ibanez, J. & Oro, J. Formaldehyde and ammonia as precursors to prebiotic amino acids. *Science* **174**, 1039-1041 (1971).

71. Fox, S. W. & Windsor, C. R. Synthesis of amino acids by heating of formaldehyde and ammonia. *Science* **170**, 984-986 (1970).

72. Oro, J., Kimball, A., Fritz, R. & Master, F. Amino acid synthesis from formaldehyde and hydroxylamine. *Arch. Biochem. Biophys.* **85**, 115-130 (1959).

73. Kamaluddin, Yanagawa, H. & Egami, F. Formation of molecules of biological interest from formaldehyde and hydroxylamine in a modified sea medium. *J. Biochem.* **85**, 1503-1508 (1979).

74. Hatanaka, H. & Egami, F. The formation of amino acids and related oligomers from formaldehyde and hydroxylamine in modified sea mediums related to prebiotic conditions. *Bull. Chem. Soc. Japan* **50**, 1147-1156 (1977).

75. Hennet, R. J. C., Holm, N. G. & Engel, M. H. Abiotic synthesis of amino acids under hydrothermal conditions and the origin of life - a perpetual phenomenon. *Naturwissenschaften* **79**, 361-365 (1992).

76. Islam, M. N., Kaneko, T. & Kobayashi, K. Determination of amino acids formed in a supercritical water flow reactor simulating submarine hydrothermal systems. *Anal. Sci.* **17**, 1631-1634 (2001).

77. Marshall, W. L. Hydrothermal synthesis of amino acids. *Geochim. Cosmochim. Acta* **58**, 2099-2106 (1994).

78. Yanagawa, H. & Kobayashi, K. An experimental approach to chemical evolution in submarine hydrothermal systems. *Origins Life Evol. Biosphere* **22**, 147-159 (1992).

79. Huber, C. & Wächtershäuser, G. α-hydroxy and α-amino acids under possible Hadean, volcanic origin-of-life conditions. *Science* **314**, 630-632 (2006).

80. Huber, C., Eisenreich, W. & Wächtershäuser, G. Synthesis of α-amino and α-hydroxy acids under volcanic conditions: implications for the origin of life. *Tetrahedron Lett.* **51**, 1069-1071 (2010).

81. Pajović, J. D. *et al*. Tryptophan-functionalized gold nanoparticles for deep UV imaging of microbial cells. *Colloids Surf. B* **135**, 742-750 (2015).

82. Cao, X. & Fischer, G. Infrared spectral, structural, and conformational studies of zwitterionic L-tryptophan. *J. Phys. Chem. A* **103**, 9995-10003 (1999).

83. Barth, A. The infrared absorption of amino acid side chains. *Prog. Biophys. Mol. Biol.* **74**, 141-173 (2000).

84. Baldermann, A. *et al.* The Fe-Mg saponite solid solution series: a hydrothermal synthesis study. *Clay Miner.* **49**, 391-415 (2014).

85. Petit, S., Baron, F. & Decarreau, A. Synthesis of nontronite and other Fe-rich smectites: a critical review. *Clay Miner.* **52**, 469-483 (2017).

86. Bakke, Ø. & Mostad, A. The structure and conformation of tryptophan in the crystal of the pure racemic compound and the hydrogen oxalate. *Acta Chem. Scand. B* **34**, 559-570 (1980).

## Supplemental Table Legend

**Supplementary Table 1 | Experimental and theoretical abiotic synthesis of amino acids at conditions of hydrothermal systems.** Aromatic amino acids are highlighted in bold. In italic is the experimental study with conditions that most resemble those of the Lost City subsurface[67]. Ala: alanine, β-Ala: beta-alanine, α-Abu: alpha-aminobutyric acid, γ-Abu: gamma-aminobutyric acid, Aca: aminocaproic acid, Ava: aminovaleric acid, Arg: arginine, Asn: asparagine, Asp: aspartic acid, Cys: cysteine, , Gln: glutamine; Glu: glutamic acid, Gly: glycine, His: histidine, Ile: isoleucine, Ise: isoserine, Leu: leucine, Lys: lysine, Met: methionine, **Phe: phenylalanine**, Pro: proline, Sar: Sarcosine, Ser: serine, Thr: threonine, **Trp: tryptophan**, **Tyr: tyrosine**, Val: valine. TC and HE stand for thermodynamic calculations and analogical hydrothermal experiments, respectively.

## Legends for Extended Data

**Extended Data Table 1 | List of TOF-SIMS fragment ions potentially characteristic of tryptophan** and detected in the region displaying the highest count rates in Fig. 3b. Only the fragment ions $C_8H_7N^+$ and $C_9H_8N^+$ (in bold) are characteristic of this amino acid while the other fragment ions can be shared with other amino acids[22]. Their small mass deviation from theoretical *m/z* values and spatial colocation allow compound identification.

**Extended Data Table 2 | Assignment for the S-FTIR bands related to organic compounds identified in the UV fluorescent saponite** (Extended Data Fig. 2). Contributions of the H-O-H bending from interlayer water at 1627 $cm^{-1}$ and of M-O-H vibration modes (with M indicating any of the cations in the structure; e.g. Mg, Fe) may interfere in the range 1500-1680 $cm^{-1}$ (ref. 15). Band assignments were taken from refs. (81-83).

**Extended Data Table 3 | Electron microprobe analyses (in wt.%) of the Fe-rich saponite encountered in the serpentinized peridotite recovered by drilling at 173.15 mbsf in the Atlantis massif.** Identification is supported by refs. (84-85). Associated mineral formulas are presented in Extended Data Table 4. Analyses were acquired in punctual mode on carbon-coated petrographic thin sections using the Cameca SX100 installed at Geosciences Montpellier (France). Operating conditions were 20 keV and 10 nA.

**Extended Data Table 4 | Fe-rich saponite formulas and associated $Fe^{3+}$ content calculated from electron microprobe analyses shown in Extended Data Table 3.**

**Extended Data Figure 1 | Large optical views of the deeply serpentinized harzburgite recovered by drilling the Atlantis massif (173.15 mbsf) during the IODP expedition 304 Leg 1309D**[12]. Both photomicrographs are centered on the two areas described in the present study (in Figs. 1-3 and 5 and in Extended Data Figs. 2 to 4 for **a** and Fig. 4 and Extended Data Fig. 5 for **b**, respectively). The high-temperature hydrated paragenesis is composed of serpentine (mesh Srp) and magnetite (Mag), both after olivine (Ol), and forming a characteristic mesh texture. Yellow to brownish phases are frequently found in the core of the mesh serpentine. They correspond to Fe-rich serpentine (Fe-Srp) and Fe-rich saponite (Sap), formed at lower temperature during secondary and tertiary alteration reactions occurring at the expense of the mesh serpentine and olivine kernels[15], some remnants of which can still be observed. Hole figures an olivine crystal removed during sample thinning and polishing. The green arrows indicate sample orientation.

**Extended Data Figure 2 | S-FTIR confirmed the presence of N-bearing organic compounds in the Fe-rich saponite** (Sap)**. a**, S-FTIR distribution maps of the aliphatic $CH_2/CH_3$ stretching band area between 2800-3000 $cm^{-1}$ shown in **c** and collected in the area indicated by the blue box in Fig. 1a. **b-c**, Associated S-FTIR spectra. The spectrum collected in the C-rich saponite (Fig. 2) shows the presence of organic compounds with modes at (1) 1270 $cm^{-1}$ and 1285 $cm^{-1}$, (2) 1380 $cm^{-1}$, (3) 1412 $cm^{-1}$, (4) 1460-1465 $cm^{-1}$, (5) 1550-1650 $cm^{-1}$, and 1728 $cm^{-1}$ in **b** and 2855, 2871, 2924 and 2858 $cm^{-1}$ in **c**. Band assignments are compiled in Extended Data Table 2. Contributions of the H-O-H bending from the saponite interlayer water at 1627 $cm^{-1}$ may interfere[15]. Also shown are the S-FTIR spectra collected in the mesh serpentine (mesh Srp) and the Fe-rich serpentine (Fe-Srp) both being nearly depleted in absorption bands related to organic

compounds. They show instead characteristic O-H stretching bands at 3570 and 3610 $cm^{-1}$ and M-O-H bending modes (with M indicating any of the cations in the hydrated silicate structure) in the range 1500-1680 $cm^{-1}$. Dotted brown curves correspond to a mixture of saponite and serpentine. Precise locations of analysis are indicated in **a** with the corresponding colored dots. FTIR spectra of protein[27] and L-tryptophan[26] are shown for comparison. "o", overtone-combination bands; "ν", stretching; "$\nu_{as}$" and "$\nu_{s}$", asymmetric and symmetric stretching, respectively; "a.u.", arbitrary unit.

**Extended Data Figure 3 | SEM image sequence illustrating FIB milling, which allowed to visualize cross-sectionally the interfaces between the C-bearing Fe-rich saponite (Sap), the Fe-rich serpentine (Fe-Srp), the mesh serpentine (mesh Srp) and the associated textures. a**, SEM-SESI view at low magnification of the UV-fluorescent area depicted in Fig. 1 and Extended Data Fig. 4; the white arrow points to the region where an ultrathin foil was milled for TEM observations (Fig. 5a-b). The green arrow provides the orientation of the sample. **b**, Enlarged SEM-SESI view of the region of interest coated with a carbon protective layer. The orange arrow designates milling direction. **c**, SEM-BSE image showing the front face of the milled section. **d**-**e**, Enlarged SEM-InLens views of the Fe-rich saponite displaying a nanoporous texture with maximum pore size of less than 100 nm, in contrast with the compact Fe-rich serpentine hosted in the mesh serpentine. Pores of the Fe-rich saponite are large enough to support the presence of a 1.2 nm sized molecule such as tryptophan[86] (see also Figs. 5a-b for associated TEM observations). **f**, Associated EDS spectra collected at 5 kV accelerating voltage. "a.u.", arbitrary unit.

**Extended Data Figure 4 | S-DUV spectral signature of the endogenous fluorescence revealed in the Fe-rich saponite. a**, Full field S-DUV image displayed in Fig. 1 and collected using an excitation wavelength ($\lambda_{exc}$) of 275 nm and a detection range of fluorescence emission between 400 and 440 nm. **b**, Fluorescence emission spectra collected with excitation wavelength of 275 nm summed from the hyperspectral datacube acquired in the area indicated by the orange box in **a** (30 s/point, 2 µm step). Fit of the S-DUV hyperspectral maps, performed using Gaussian functions and 10 iterations, resolved 4 main contributions at 340±6, 358±3, 380±3 and 403±3 nm. **c**, Associated spatial distributions of fluorescence emissions at 340, 358, 380 and 403 nm. They revealed systematic colocalization of these 4 components. The green arrows indicate sample orientation. “a.u.”, arbitrary unit.

**Extended Data Figure 5 | SEM image sequence illustrating FIB milling, which allowed to visualize cross-sectionally the interfaces between the UV-fluorescent Fe-rich saponite (Sap), the olivine kernel (Ol) and the mesh serpentine (mesh Srp). a**, SEM-SESI view at low magnification of the UV-fluorescent area shown in Fig. 4; the white arrow points to the region of interest where an ultrathin foil was milled for TEM observations (Fig. 4d). The green arrow indicates the orientation of the sample. **b**, SEM-SESI view of the region of interest coated with a carbon protective layer. The orange arrow designates the milling direction. **c**, SEM-SEI image showing the FIB milled trench at the leading edge of the region of interest. **d**, SEM-BSE image showing the front face of the milled section. Similarly to Extended Data Fig. 3, it revealed marked textural contrasts between the mineral phases, the Fe-rich saponite presenting the highest porosity.

**Extended Data Figure 6 | Enlarged views of the positive TOF-SIMS spectra collected in the Fe-rich saponite. a-n**, Enlarged views of the positive TOF-SIMS spectrum from Fig. 3d reconstructed from the region displaying the highest count rate. **i-n**, Selected close up views of this TOF-SIMS spectrum showing regions where the peaks of fragment ions characteristic of isoprenoids such as pristane ($C_{19}H_{40}$), squalane ($C_{30}H_{50}$) and lycopane ($C_{40}H_{56}$) along with polycyclic compounds (cholestane, $C_{27}H_{48}$; β-carotane, $C_{40}H_{56}$ and hopanoids) should be found if present[23-25]. These biomarkers were previously detected using gas chromatography in the bulk rock[13] but are not detected locally in our mineral assemblage. **o-v**, Enlarged views of the positive TOF-SIMS spectra reconstructed from the region displaying the highest count rate in Fig. 4f. **a-c** and **o-q** exhibit peaks of fragments ions characteristic of siloxane, a common plasticizer contaminant. No significant peaks can be found in the 350-450 *m/z* regions (**d**, **e**, **r**, and **s**) where the aliphatic fraction (including fragment ions from the sterane and hopane classes and from alkanes and monocyclic alkanes) is expressed in positive TOF-SIMS spectra[23-25].

**Extended Data Figure 7 | Chemical affinity as a function of the logarithm of the activity of aqueous dihydrogen ($H_{2(aq)}$) for the reactions corresponding to the abiotic synthesis of pyruvate ($C_3H_3O_3^-$), indole ($C_8H_7N$), and tryptophan ($C_{11}H_{12}N_2O_2$)** (Supplementary Information)**.** The vertical lines indicate the range of $H_2$ activities reported for the moderate-temperature fluids of the Lost City hydrothermal field[39].

**Extended Data Figure 8 | Activity diagram of aqueous hydrogen ($H_{2(aq)}$) depicting, as a function of pH, the fields of relative predominance of nitrogen species (*i.e.* ammonium, $NH_4^+$, aqueous ammonia, $NH_{3(aq)}$, and aqueous dinitrogen, $N_{2(aq)}$) at 200°C and 150 bar and**

**considering a total nitrogen amount ($\sum$ N) of $6 \cdot 10^{-6}$ M.** The limits between two predominance fields have been drawn for equal activities of the nitrogen species. The dark blue star indicates conditions encountered at depth in the Atlantis massif by considering a mean $H_2$ activity of 10.5 mM[39] and a pH of 7.12 calculated with tremolite-chrysotile-diopside as the alteration assemblage consistent with hydrothermal fluid composition[38]. The activity of water was assumed equal to 1. Diagram shows that $NH_{3(aq)}$ is thermodynamically favored at 200°C. QFM: quartz-fayalite-magnetite mineral buffer.

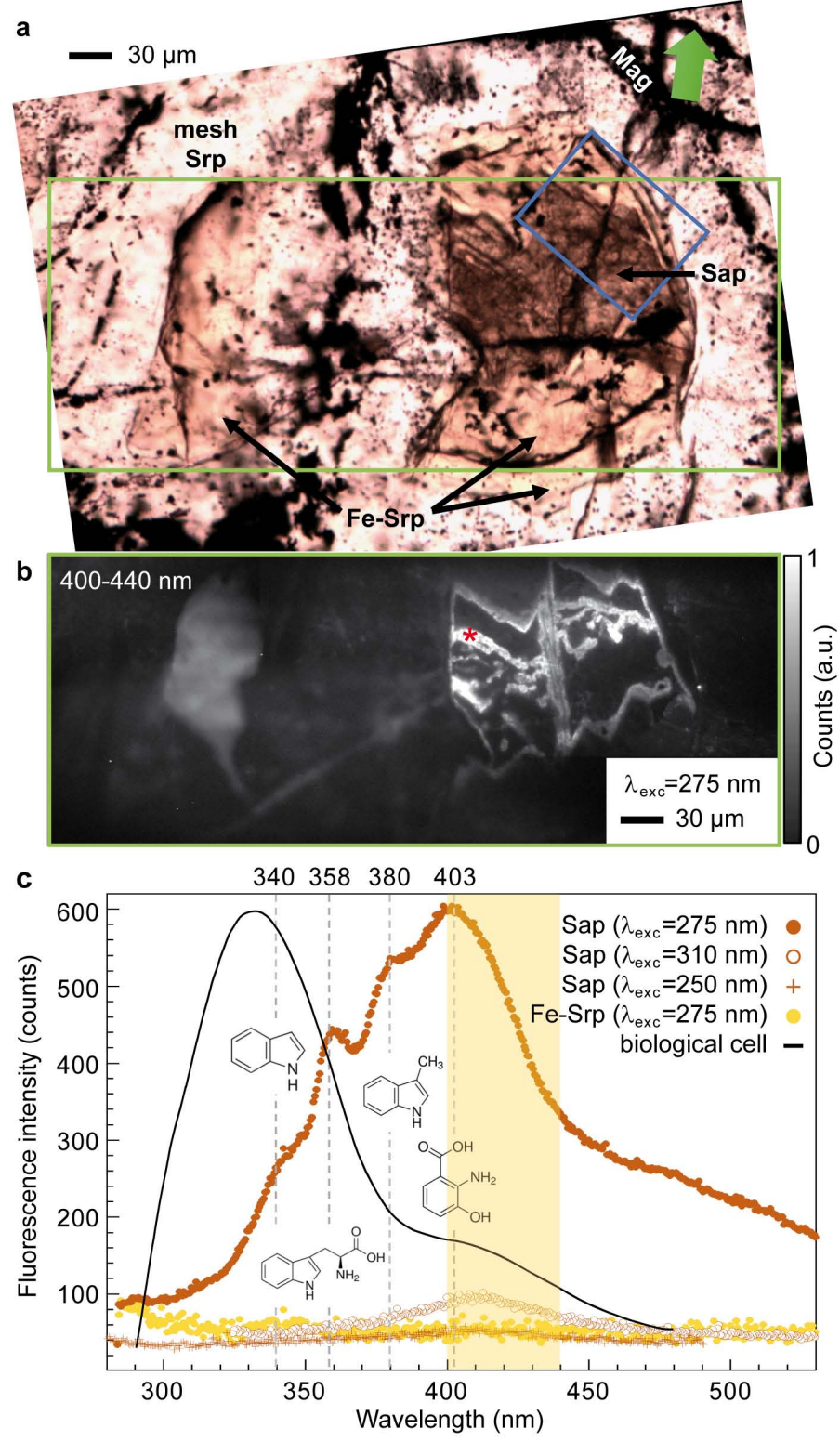
a
30 µm
Mag
mesh
Srp
Sap
Fe-Srp
b
400-440 nm
*
λexc=275 nm
30 µm
1
Counts (a.u.)
0
c
340
358
380
403
Sap (λexc=275 nm)
Sap (λexc=310 nm)
Sap (λexc=250 nm)
Fe-Srp (λexc=275 nm)
biological cell
Fluorescence intensity (counts)
Wavelength (nm)
600
500
400
300
200
100
300
350
400
450
500
N
H
CH3
OH
NH2

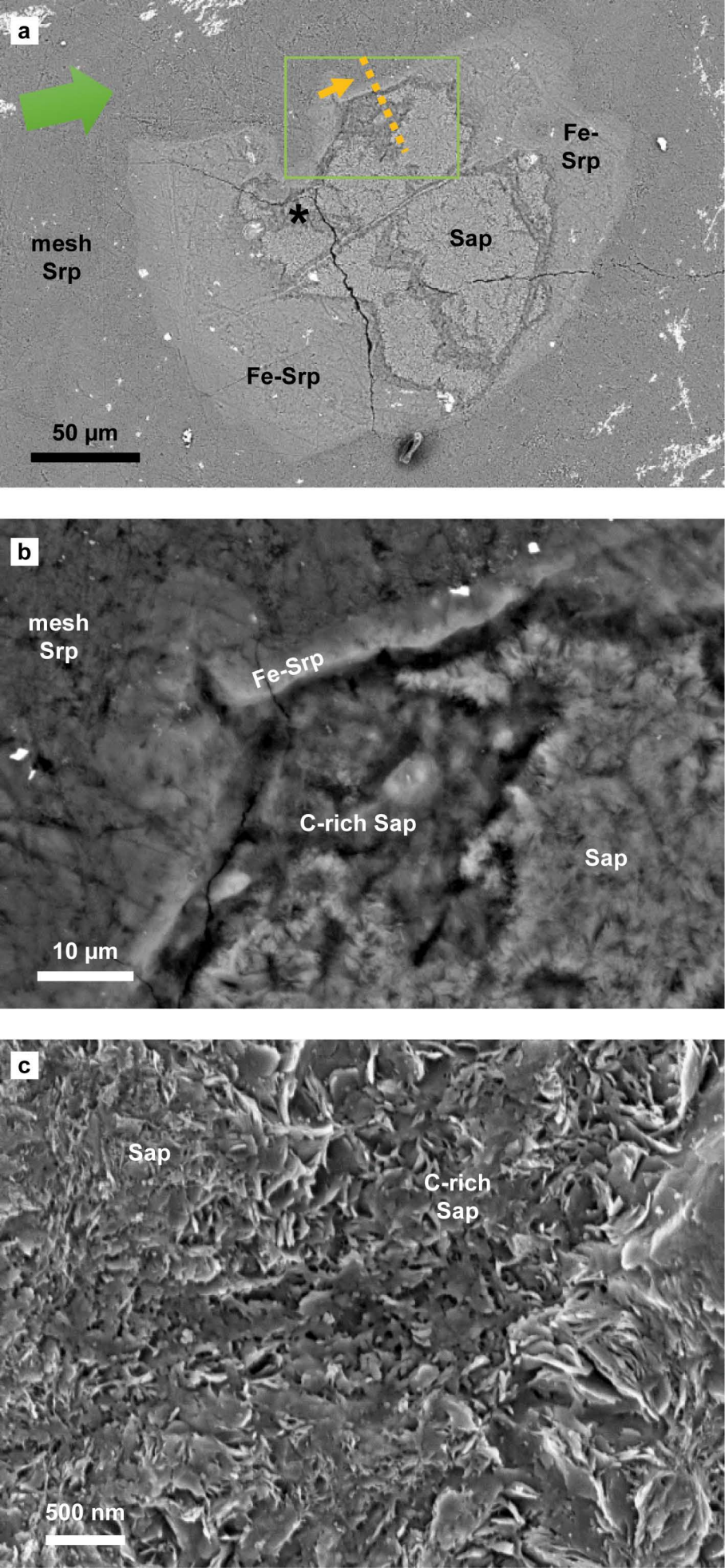
a
Fe-
Srp
*
mesh
Srp
Sap
Fe-Srp
50 µm
b
mesh
Srp
Fe-Srp
C-rich Sap
Sap
10 µm
c
Sap
C-rich
Sap
500 nm

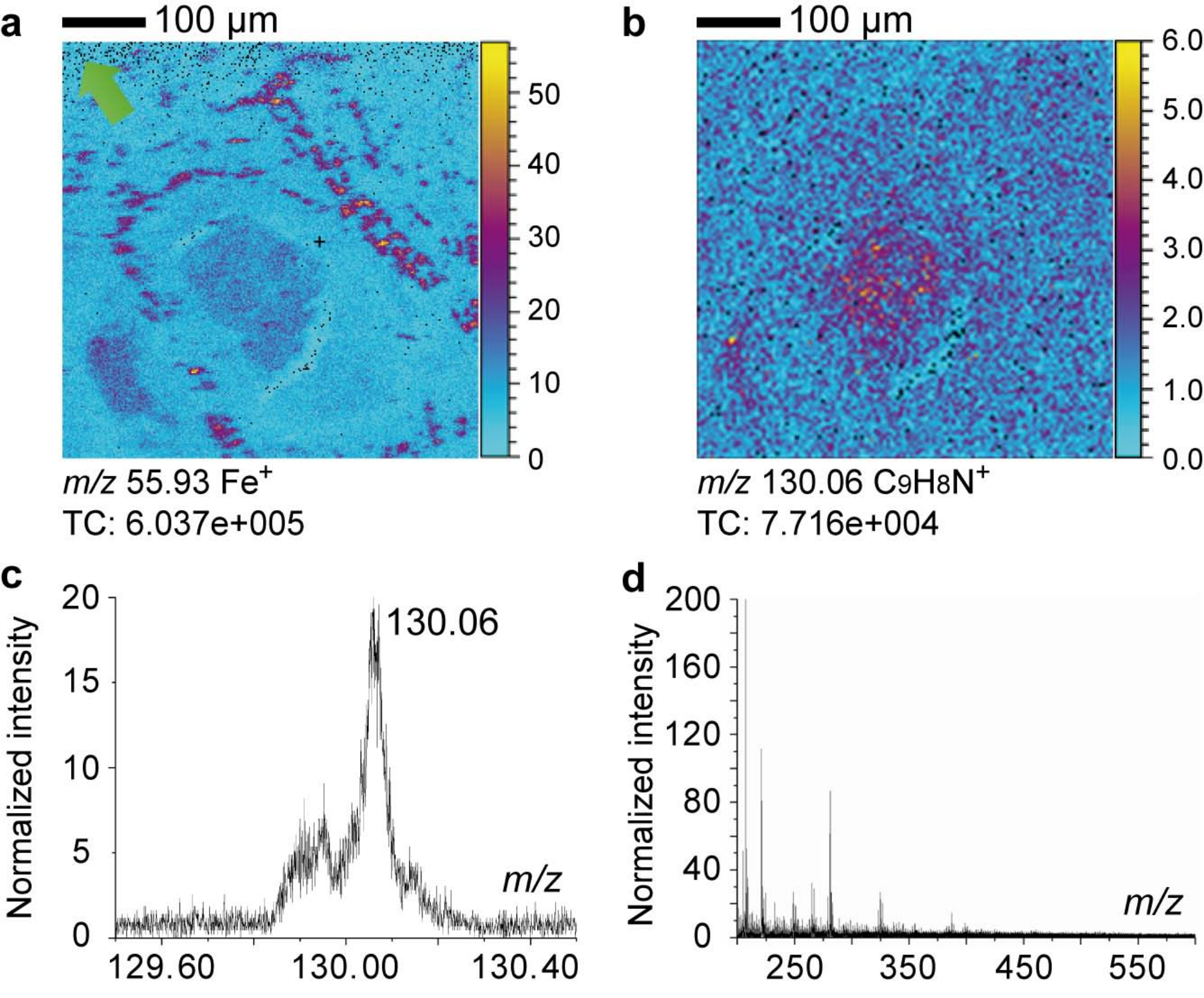
a
100 µm
50
40
30
20
10
0
m/z 55.93 Fe+
TC: 6.037e+005
b
100 µm
6.0
5.0
4.0
3.0
2.0
1.0
0.0
m/z 130.06 C9H8N+
TC: 7.716e+004
c
Normalized intensity
20
15
10
5
0
130.06
m/z
129.60
130.00
130.40
d
Normalized intensity
200
160
120
80
40
0
m/z
250
350
450
550

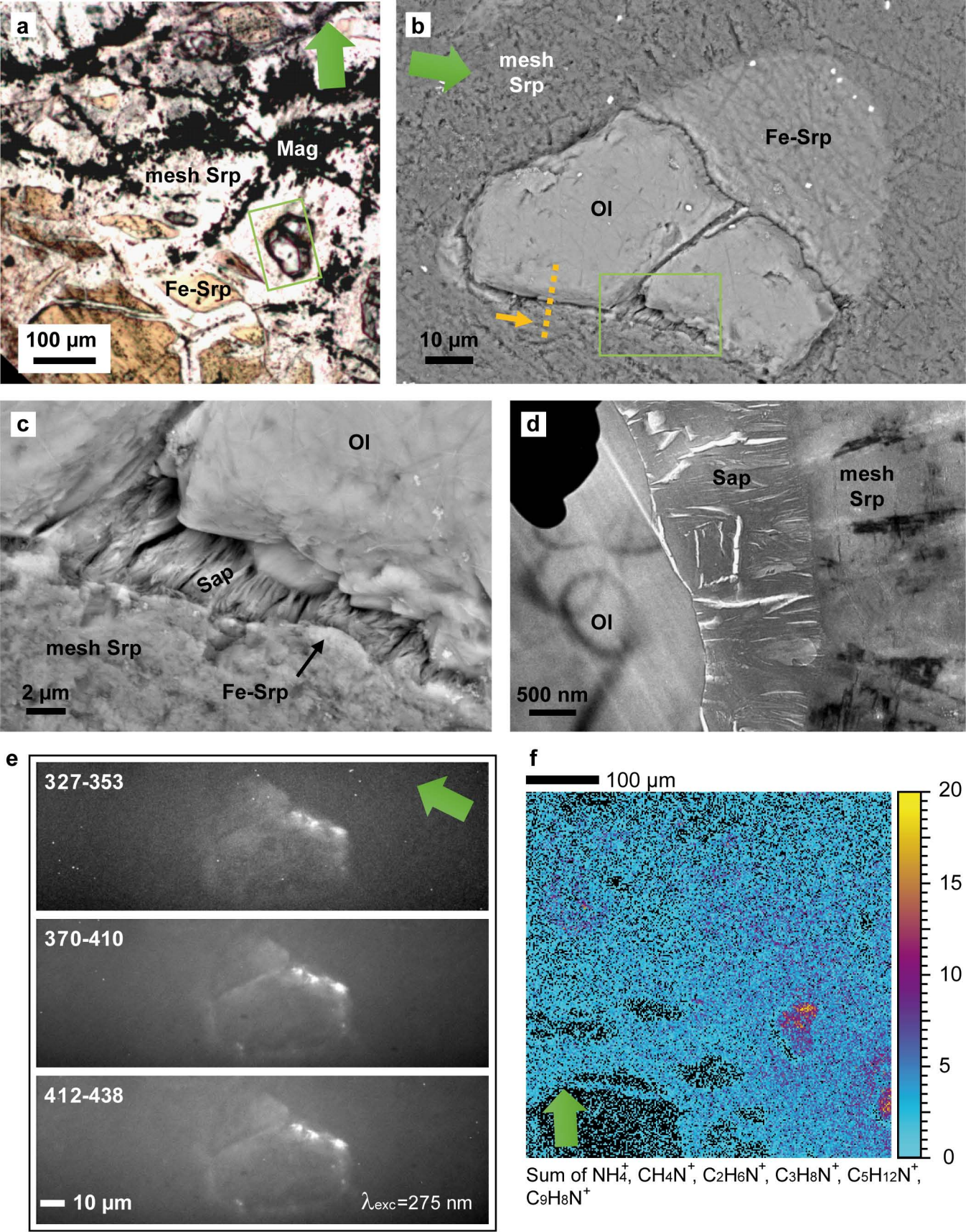
a
Mag
mesh Srp
Fe-Srp
100 µm
b
mesh
Srp
Fe-Srp
Ol
10 µm
c
Ol
Sap
mesh Srp
Fe-Srp
2 µm
d
Sap
mesh
Srp
Ol
500 nm
e
327-353
370-410
412-438
10 µm
λexc=275 nm
f
100 µm
20
15
10
5
0
Sum of NH4+, CH4N+, C2H6N+, C3H8N+, C5H12N+, C9H8N+

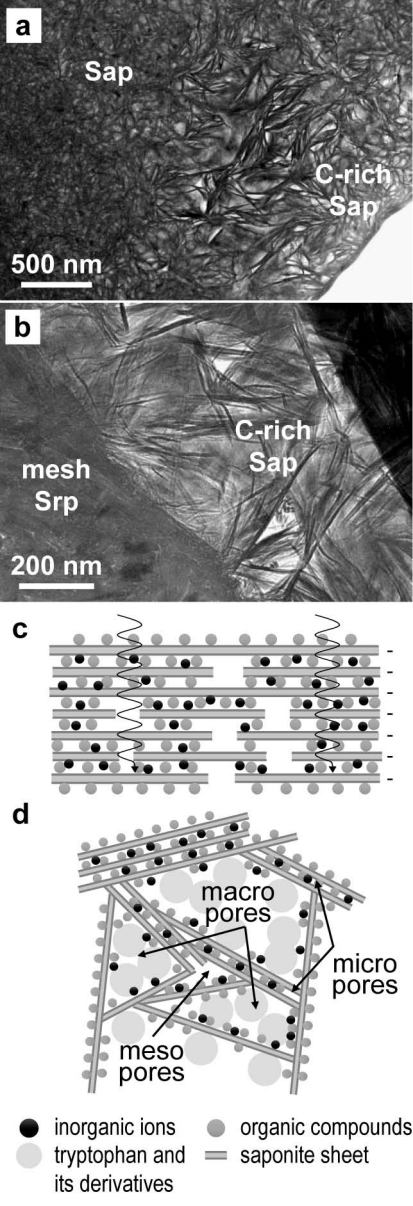
a
Sap
C-rich
Sap
500 nm
b
C-rich
Sap
mesh
Srp
200 nm
c
d
macro
pores
micro
pores
meso
pores
inorganic ions
organic compounds
tryptophan and
its derivatives
saponite sheet